Efficient Polarization Demosaicking Via Low-Cost Edge-Aware and Inter-Channel Correlation

Guangsen Liu, Peng Rao, Xin Chen, Yao Li, and Haixin Jiang

***Abstract*—Efficient and high-fidelity polarization demosaicking is critical for the industrial applications of division of focal plane (DoFP) polarization imaging systems. However, existing methods often struggle to balance speed, accuracy, and complexity. This study introduces a novel polarization demosaicking algorithm that interpolates DoFP images within a three-stage basic demosaicking framework. Our method incorporates a DoFP low-cost edge-aware technique (DLE) to guide the interpolation process. Furthermore, inter-channel correlation is used to calibrate the initial estimate in the polarization difference domain. The proposed algorithm is available in both lightweight and full versions, designed for different application requirements. Experiments on simulated and real DoFP images demonstrated that both versions achieve the highestt interpolation accuracy and speed, respectively, among existing interpolation-based algorithms and significantly enhanced visuals. The lightweight and full versions efficiently processed a 1024 × 1024 image on an AMD Ryzen 5600X CPU in 0.1402s and 0.2693s, respectively. Additionally, as our methods operate within a 5 × 5 window, parallel acceleration on graphics processing units (GPUs) or field-programmable gate arrays (FPGAs) is highly feasible.**

***Index Terms*—Polarization demosaicking, polarization remote sensing, division of focal plane (DoFP), interpolation, edge-aware, inter-channel correlation, polarization image dataset.**

I. Introduction

POLARIZATION, a fundamental property of light, reveals several characteristics such as surface roughness [1], three-dimensional normals [2], and material composition [3] of objects. Hence, polarization imaging technology that captures this information has been widely applied across various fields, including autonomous driving [4], target detection [5], three-dimensional reconstruction [6], material identification [7], defogging [8], and biomedical imaging [9].

Advancements in polarimetric imaging sensor technology have increased the importance of the division of focal plane (DoFP) polarimetry in various polarimetric imaging systems, owing to its miniaturisation and real-time data acquisition capabilities. However, DoFP polarization imagers inherently compromise spatial resolution to facilitate the simultaneous acquisition of high-temporal-resolution optical signals from multiple polarization channels. DoFP cameras incorporate a polarization filter array (PFA) with orientations of 0°, 45°, 90°, and 135° emulating the pixel arrangement within the colour filter array (CFA) (Fig. 1). Consequently, DoFP faces challenges akin to those encountered by CFA, particularly in the complex task of reconstructing a full polarization image from incomplete channel data. Such reconstruction necessitates that for each pixel of a DoFP image, the information from the remaining three channels must be accurately inferred to construct a complete description of the polarization state.

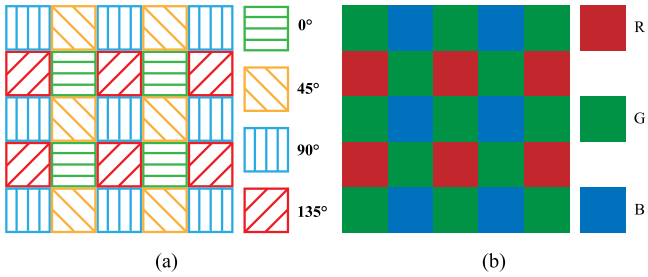

Fig. 1. Schematic of the patterns of (a) a 5×5 PFA and (b) a 5×5 CFA.

Although colour demosaicking has been extensively researched, yielding numerous efficient algorithms [10], [11], [12], [13], [14], [15], these methods cannot be directly applied to polarization demosaicking owing to the distinct channel distributions and correlations present in this task [16].

Numerous interpolation-based algorithms have been developed for demosaicking DoFP images to mitigate instantaneous field of view (IFoV) errors [17] and enhance spatial resolution. Traditional methods such as the nearest-neighbour (NN), bilinear (BI), and bicubic (BCB) [18] algorithms perform interpolations on individual channels. As low-pass filters, these techniques often generate pronounced artefacts in high-frequency parts. Zhang et al. [19] introduced an algorithm employing intensity correlation among polarization channels (ICPC) that identifies edges and interpolates images along a single direction. However, this binary decision approach is prone to significant information loss. Li et al. [20] proposed Newton's polynomial (NP) interpolation method to diminish artefacts and reduce information loss via weighted interpolations within the polarization difference domain. This method though

Received 10 October 2024; revised 9 November 2024; accepted 14 November 2024. Date of publication 19 November 2024; date of current version 31 December 2024. *(Corresponding author: Peng Rao.)*

Guangsen Liu, Yao Li, and Haixin Jiang are with the University of Chinese Academy of Sciences, Beijing 100049, China, and also with the Key Laboratory of Intelligent Infrared Perception and Shanghai Institute of Technical Physics, Chinese Academy of Sciences, Shanghai 200083, China (e-mail: liuguangsen20@mails.ucas.ac.cn; liyao201@mails.ucas.ac.cn; jianghaixin22@mails.ucas.ac.cn).

Peng Rao and Xin Chen are with the Shanghai Institute of Technical Physics, Chinese Academy of Sciences, Shanghai 200083, China, and also with the Key Laboratory of Intelligent Infrared Perception, Chinese Academy of Sciences, Shanghai 200083, China (e-mail: peng_rao@mail.sitp.ac.cn; chenxin@mail.sitp.ac.cn).

Digital Object Identifier 10.1109/JPHOT.2024.3502117

advantageous, requires a manually set, fixed decision threshold, leading to the potential over- or under-estimation of pixel values. Morimatsu et al. [21] developed the edge-aware residual interpolation (EARI) technique, which utilizes an intensity map as a base for guided filtering in the residual domain, enhancing interpolation precision, but at a significantly higher cost. Algorithms based on inter-channel correlation, such as PCDP [22], maintain low computational overhead by retaining only convolutional operations; nonetheless, they neglect directional interpolation, leading to visual errors, such as the 'zip' effect, and mediocre performance on metrics such as peak signal to noise ratio (PSNR), root mean squared error (RMSE), and structural similarity index measure (SSIM). Polarization demosaicking using edge compensation (PDEC) [23] addresses this by applying a single-channel Hamilton–Adam (HA) interpolation on bilinear-interpolated images. However, this merely blurs IFoV errors without genuinely resolving the loss of information during the interpolation process. These challenges highlight the importance of selecting appropriate interpolation directions for reconstructing high-precision polarization images. Despite extensive studies, existing interpolation-based DoFP demosaicking methods still suffer from high computational costs and insufficient image quality in real-time applications.

Optimization-based and data-driven algorithms have emerged as focal points in recent studies. The sparse representation method [24] yields significant improvements in demosaicking; however, its computational complexity limits its applicability to real-time imaging. Deep learning-based demosaicking [25], [26], [27] has advanced considerably; however, training such models requires high-quality data and substantial computational resources. Moreover, simultaneously acquiring DoFP and ground-truth images remains challenging. These issues constrain the broad industrial adoption of deep learning techniques for DoFP demosaicking.

Summarily, although current demosaicking methods strive for simplicity, accuracy, and real-time execution, they still face challenges in balancing complexity, precision, and speed effectively.

This study developed a demosaicking method that reduces computational overhead while enhancing image quality, particularly for industrial applications. Our main contributions are as follows:

1) We introduced a three-stage interpolation-based polarization demosaicking framework (TIPDF) to standardise the interpolation steps for four-channel DoFP images. This framework is divided into three primary phases: estimation of orthogonal channel planes, determination of non-orthogonal channel planes, and refinement of interpolation results.
2) We developed a novel polarization demosaicking algorithm that employs a low-cost edge-aware and inter-channel correlation (LEIC) method to facilitate rapid high-quality reconstruction of DoFP polarization images. Our algorithm integrated a DoFP low-cost edge-aware (DLE) technique to enable rapid interpolation decisions and an inter-channel correlation calibration (ICCC) to refine the initial estimates. For applications, a lighter version of LEIC, low-cost edge-aware polarization demosaicking (LEPD) was introduced. We presented comprehensive quantitative assessments and visual comparisons of our reconstruction with other established algorithms using publicly available datasets.
3) We created an outdoor long-wave infrared and visible DoFP polarization image dataset (OLVD), which includes thousands of LWIR and VIS DoFP images captured simultaneously or individually. Several scenes of OLVD were used to evaluate the effectiveness of different demosaicking methods on real DoFP images. The dataset will provide a valuable contribution to subsequent research.

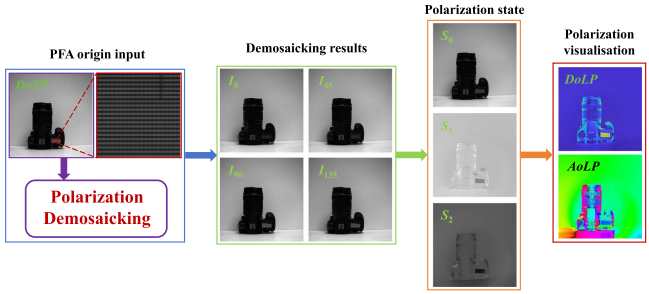

Fig. 2. Reconstruction workflow for DoFP polarization images.

II. Linear Polarization Calculation

The DoFP detector acquires polarization images by capturing light through four distinct polarization filters. The polarization state of light can be represented by a Stokes vector, denoted as $S = [S_0, S_1, S_2, S_3]$. The first three components of S are defined as follows [27]:

$$S_0 = 0.5(I_0 + I_{45} + I_{90} + I_{135}), \tag{1a}$$

$$S_1 = I_0 - I_{90}, \tag{1b}$$

$$S_2 = I_{45} - I_{135}, \tag{1c}$$

where I_θ represents the intensities measured by the DoFP detector at polarization angles of θ, S_0 corresponds to the total intensity of incident light, and S_1 and S_2 correspond to the linear polarization components. The degree of linear polarization ($DoLP$) and angle of linear polarization ($AoLP$) are commonly used to describe polarization attributes, which are expressed as

$$DoLP = \frac{\sqrt{S_1^2 + S_2^2}}{S_0}, \tag{2a}$$

$$AoLP = 0.5 \arctan\left(\frac{S_2}{S_1}\right). \tag{2b}$$

The process of reconstructing and visualizing polarization images is shown in Fig. 2.

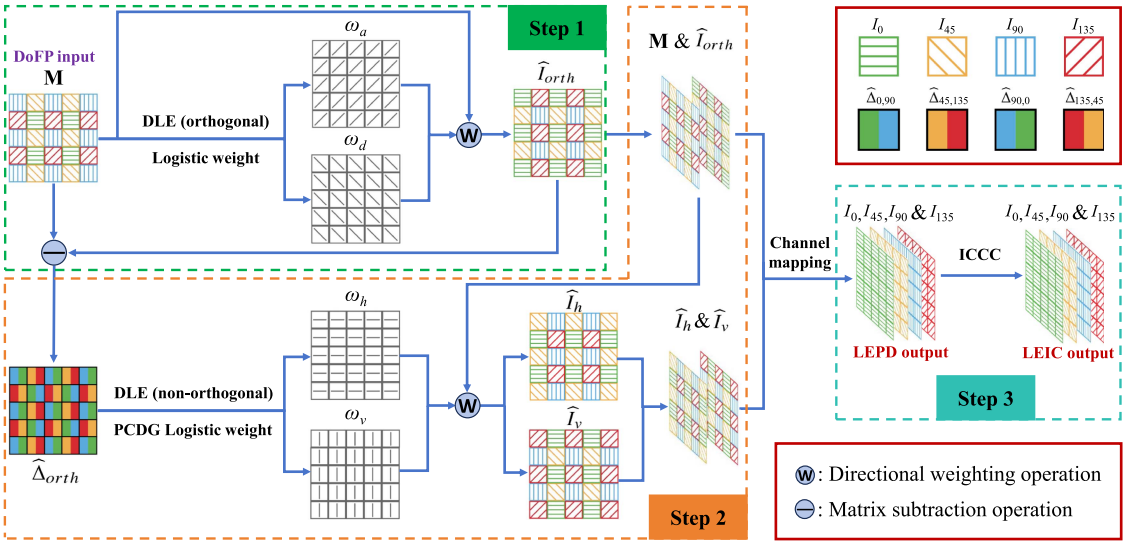

Fig. 3. Flowchart illustrating our polarization demosaicking process. Steps 1 to 3 each correspond to the three stages of TIPDF.

III. Polarization Demosaicking Using Low-Cost Edge-Aware and Inter-Channel Correlation

In this section, we elaborate on the technical details of the demosaicking algorithm developed in this study. Initially, we introduce a TIPDF to guide the demosaicking process. Subsequently, detailed computations are provided for the DLE technique, orthogonal and non-orthogonal channel plane estimation, and ICCC. A flowchart illustrating our polarization demosaicking process is shown in Fig. 3.

A. Polarization Demosaicking Framework

The TIPDF is proposed to standardise the DoFP demosaicking operation (Fig. 3). For a single DoFP image, missing pixels are completed in the first two stages based on edge awareness, and in the third stage the results are corrected using the observed pixels of DoFP.

For PFA, the orthogonal channel pixels are arranged centrosymmetrically among the neighbouring pixels of the interpolated pixel, facilitating directional interpolation. Therefore, the missing orthogonal channel values corresponding to each pixel are estimated first, ensuring that half the pixels in each channel plane have values. Subsequently, both the DoFP and orthogonal channel planes are utilized to estimate the remaining two channels, compensating for the missing pixels across all channels. This approach is inspired by NP [20], which has been well used for industrial polarimetric imaging. However, applying edge awareness in polarization demosaicking requires addressing specific challenges, and we have implemented targeted optimizations based on the TIPDF framework.

Edge detection and weight calculation are both time-consuming and complex processes [20], [21]. To address this, we introduce DLE technology for efficient and flexible edge awareness. In the second stage, we propose the concept of polarization channel difference gradient (PCDG) and use the PCDG graph to guide edge determination.

In addition, because the correlation of the non-orthogonal channels is stronger than that of the orthogonal channel, prioritizing interpolation for the orthogonal channel may introduce certain errors. The observed pixels of the DoFP image represent the only accurate pixel information available. To maximize their effectiveness, inter-channel correlation [22], [23] is employed to further calibrate the polarization image, enhancing the overall accuracy of the demosaicking process.

B. DoFP Low-Cost Edge-Aware

The Hamilton–Adams demosaicking algorithm (HA) is widely recognized for demosaicking CFA images owing to its ability to achieve notable results through simple computations [28], [29], [30]. We adapted the HA algorithm for PFA images to streamline the interpolation decision-making process. The application of the HA algorithm in orthogonal channels is detailed below.

Consider $\mathbf{M}$, the original DoFP image, consisting of m rows and n columns. The set of all pixel coordinates is defined as follows:

$$L = \{(i,j) \in \mathbb{N}^2 | i \in [1,m], j \in [1,n]\}. \tag{3}$$

First, the computations of first and second-order diagonal and anti-diagonal partial derivatives of image $\mathbf{M}$ are conducted as follows:

$$\partial_d \mathbf{M}(i,j) = \frac{\mathbf{M}(i+1,j+1) - \mathbf{M}(i-1,j-1)}{2\sqrt{2}}, \tag{4a}$$

$$\partial_d^2 \mathbf{M}(i,j) = \frac{\mathbf{M}(i+2,j+2) + \mathbf{M}(i-2,j-2) - 2\mathbf{M}(i,j)}{8}, \tag{4b}$$

$$\partial_a \mathbf{M}(i,j) = \frac{\mathbf{M}(i-1,j+1) - \mathbf{M}(i+1,j-1)}{2\sqrt{2}}, \tag{4c}$$

$$\partial_a^2\mathbf{M}(i,j) = \frac{\mathbf{M}(i-2,j+2)+\mathbf{M}(i+2,j-2)-2\mathbf{M}(i,j)}{8}, \tag{4d}$$

where d and a denote the diagonal and anti-diagonal directions, respectively.

Next, we calculate the local intensity variations as follows:

$$v_d = |\partial_d\mathbf{M}(i,j)| + \left|2\sqrt{2}\partial_d^2\mathbf{M}(i,j)\right|, \tag{5a}$$

$$v_a = |\partial_a\mathbf{M}(i,j)| + \left|2\sqrt{2}\partial_a^2\mathbf{M}(i,j)\right|. \tag{5b}$$

The average of the neighbouring orthogonal channels in the diagonal and anti-diagonal directions are expressed as

$$\overline{I}_{orth}^{d} = \frac{1}{2}(\mathbf{M}(i+1,j+1)+\mathbf{M}(i-1,j-1)), \tag{6a}$$

$$\overline{I}_{orth}^{a} = \frac{1}{2}(\mathbf{M}(i+1,j-1)+\mathbf{M}(i-1,j+1)). \tag{6b}$$

Further, the estimation of the orthogonal channel value at a given position (i,j) is expressed as

$$\widehat{I}_{orth}(i,j) = \omega_d(\overline{I}_{orth}^{d} - \partial_d^2\mathbf{M}(i,j)) + \omega_a(\overline{I}_{orth}^{a} - \partial_a^2\mathbf{M}(i,j)), \tag{7}$$

where ω_d and ω_a denote the interpolation weights in the diagonal and anti-diagonal directions, respectively. These weights are determined based on the variations v_d and v_a and satisfy the normalization condition $\omega_d + \omega_a = 1$.

C. Orthogonal Channel Plane Estimation

The DLE is initially employed to estimate the values of the orthogonal channels; these values can then be used to construct the orthogonal channel plane. In certain previous demosaicking methods, edge detection primarily depended on a basic ternary edge classifier [11], [28]:

$$\omega_d = \begin{cases} 0 & \text{if } v_d - v_a < -T \\ 1 & \text{if } v_d - v_a > T \\ 0.5 & \text{if } |v_d - v_a| \le T \end{cases}. \tag{8}$$

However, a limitation of this approach is the selection of the threshold T for different scenarios. An improperly chosen T can result in conflicting estimation results. Therefore, a continuous function $f(v_d - v_a)$ is used to represent ω_d. In this study, we use the logistic function to calculate ω_d as follows:

$$\omega_d = f(v_d - v_a) = \frac{1}{1+e^{k(v_d - v_a)}}, \tag{9a}$$

$$k = k_0\frac{255}{DR(\mathbf{M})}, \tag{9b}$$

where k is a parameter used to modify the change in weights. The logistic function ensures a continuous adjustment of the weights, preventing the incorrect decisions that can occur with a step function. Furthermore, $\omega_a = f(v_a - v_d) = 1 - \omega_d$, an equivalent form of calculation for both weights. Given the inverse relationship between k and the range of $(v_d - v_a)$ and the direct relationship between $(v_d - v_a)$ and the dynamic range of the DoFP image $DR(\mathbf{M})$, k is inversely proportional to $DR(\mathbf{M})$. The value of k_0 represents k when $DR(\mathbf{M}) = 255$. Experimental results using a range of k_0 values ranging from 0.1 to 10.0 with a step size of 0.1 on Qiu et al.'s dataset [31] revealed that the optimal PSNR was obtained at $k_0 = 1.0$. Thus, in this study, $k_0 = 1.0$ is adopted.

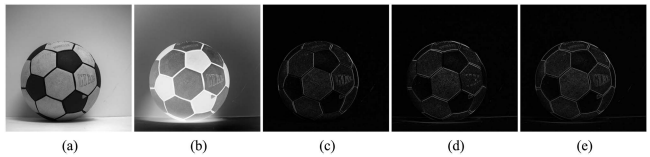

Fig. 4. Visualization of polarization channel difference gradients (PCDG). (a) DoFP image. (b) Visualization of orthogonal polarization channel difference. (c) PCDG in the horizontal direction. (d) PCDG in the vertical direction. (e) Absolute PCDG.

Equation (7) utilizes the weights formulated in (9) to estimate the orthogonal channel plane $\widehat{I}_{orth}$. The continuity of the logistic function will help the DLE to make flexible interpolation decisions, which is the key to ensuring interpolation accuracy in low-cost edge-aware process.

D. Non-Orthogonal Channel Plane Estimation

In a DoFP image, the horizontal and vertical neighbouring pixels of each pixel correspond to different polarization channels. Relying solely on the observed values for estimation inevitably results in the loss of valuable information from the other direction. The orthogonal channel plane addresses this information loss, compensating for it by utilizing the fact that the horizontal and vertical neighbouring pixels are channels orthogonal to each other.

In CFA demosaicking, chrominance gradients are steeper in the direction perpendicular to edges than that parallel to them [32]. We adopted this perspective for DoFP images, indicating that the polarization channel difference gradient (PCDG) is significant in the trans-edge direction (Fig. 4). In this study, PCDG serves as a reliable parameter for reflecting edges and is utilized for edge-aware processing in horizontal and vertical channels.

First, the orthogonal channel difference map is formulated as

$$\widehat{\Delta}_{orth}(i,j) = \mathbf{M}(i,j) - \widehat{I}_{orth}(i,j). \tag{10}$$

The first and second-order horizontal and vertical partial derivatives of the orthogonal channel residual map are computed as

$$\partial_h\widehat{\Delta}_{orth}(i,j) = \frac{\widehat{\Delta}_{orth}(i,j+1) - \widehat{\Delta}_{orth}(i,j-1)}{2}, \tag{11a}$$

$$\partial_h^2\widehat{\Delta}_{orth}(i,j) = \frac{\widehat{\Delta}_{orth}(i,j+2) + \widehat{\Delta}_{orth}(i,j-2) - 2\widehat{\Delta}_{orth}(i,j)}{4}, \tag{11b}$$

$$\partial_v\widehat{\Delta}_{orth}(i,j) = \frac{\widehat{\Delta}_{orth}(i+1,j) - \widehat{\Delta}_{orth}(i-1,j)}{2}, \tag{11c}$$

$$\partial_v^2\widehat{\Delta}_{orth}(i,j)$$

$$= \frac{\widehat{\Delta}_{orth}(i+2,j) + \widehat{\Delta}_{orth}(i-2,j) - 2\widehat{\Delta}_{orth}(i,j)}{4}, \quad (11d)$$

where h and v represent the horizontal and vertical directions, respectively.

Next, PCDGs related to edge variations in the horizontal and vertical directions are computed as follows:

$$v_h = \left|\partial_h \widehat{\Delta}_{orth}(i,j)\right| + \left|2\partial_h^2 \widehat{\Delta}_{orth}(i,j)\right|, \quad (12a)$$

$$v_v = \left|\partial_v \widehat{\Delta}_{orth}(i,j)\right| + \left|2\partial_v^2 \widehat{\Delta}_{orth}(i,j)\right|. \quad (12b)$$

Subsequently, the average of the neighbouring horizontal and vertical channels in the horizontal and vertical directions is calculated from the DoFP plane and orthogonal channel plane by

$$\overline{I}_h^h = \frac{1}{2}(\mathbf{M}(i,j+1) + \mathbf{M}(i,j-1)), \quad (13a)$$

$$\overline{I}_h^v = \frac{1}{2}(\widehat{I}_{orth}(i+1,j) + \widehat{I}_{orth}(i-1,j)), \quad (13b)$$

$$\overline{I}_v^h = \frac{1}{2}(\widehat{I}_{orth}(i,j+1) + \widehat{I}_{orth}(i,j-1)), \quad (13c)$$

$$\overline{I}_v^v = \frac{1}{2}(\mathbf{M}(i+1,j) + \mathbf{M}(i-1,j)), \quad (13d)$$

where the subscript of $\overline{I}$ represents the channel, h denotes a horizontal neighbour, and v denotes a vertical neighbour with respect to the interpolated pixel; the superscript refers to the direction of interpolation.

Similar to (4b) and (4d), the second-order horizontal and vertical partial derivatives of DoFP are computed as

$$\partial_h^2 \mathbf{M}(i,j) = \frac{\mathbf{M}(i,j+2) + \mathbf{M}(i,j-2) - 2\mathbf{M}(i,j)}{4}, \quad (14a)$$

$$\partial_v^2 \mathbf{M}(i,j) = \frac{\mathbf{M}(i+2,j) + \mathbf{M}(i-2,j) - 2\mathbf{M}(i,j)}{4}. \quad (14b)$$

Finally, the value of horizontal and vertical channels at position (i,j) are estimated by

$$\widehat{I}_h(i,j) = \omega_h(\overline{I}_h^h - \partial_h^2 \mathbf{M}(i,j)) + \omega_v(\overline{I}_h^v - \partial_v^2 \mathbf{M}(i,j)), \quad (15a)$$

$$\widehat{I}_v(i,j) = \omega_h(\overline{I}_v^h - \partial_h^2 \mathbf{M}(i,j)) + \omega_v(\overline{I}_v^v - \partial_v^2 \mathbf{M}(i,j)), \quad (15b)$$

$$\omega_h = f(v_h - v_v) = \frac{1}{1 + e^{k(v_h - v_v)}}, \quad (15c)$$

$$\omega_v = f(v_v - v_h) = \frac{1}{1 + e^{k(v_v - v_h)}} = 1 - \omega_h, \quad (15d)$$

where ω_h and ω_v denote the horizontal and vertical directional weights, respectively, and k is calculated by (9b), with parameter $k_0 = 1.0$, as introduced in Section III-C.

At this point, we deduce estimates for the remaining three channels at the location (i,j): $\widehat{I}_{orth}(i,j)$, $\widehat{I}_h(i,j)$ and $\widehat{I}_v(i,j)$.

These estimates are extended across the entire image and successively mapped onto each polarization channel plane to obtain the concatenation of demosaicked images: $[\widehat{I}_0, \widehat{I}_{45}, \widehat{I}_{90}, \widehat{I}_{135}]$.

E. Calibration With Inter-Channel Correlation

Following the aforementioned process, we obtained the demosaicked images of the four channels. Three channels are interpolated independently, as the complementary of each pixel, and fidelity can be further enhanced using the ICCC technique.

ICCC is based on a difference plane interpolation technique commonly employed in CFA demosaicking [33], [34]. It leverages colour correlation to significantly improve interpolation precision by focusing on the difference plane, which mitigates interpolation inaccuracies introduced by the high-frequency content of the image. The efficacy of this method has been validated in DoFP demosaicking applications [22], [23].

Given the strong correlation among polarization channels [23], calibrations through ICCC involve mutual referencing among the four pre-interpolated images. The method initially estimates the mean local polarization channel differences and subsequently adjusts their interpolation to refine the overall image quality. The details are as follows:

For an individual channel x ($x \in \{0, 45, 90, 135\}$), a sparse raw plane $\widetilde{\mathbf{M}}_x$ is computed by

$$\widetilde{\mathbf{M}}_x = \mathbf{M} \odot mask_x, \quad (16)$$

where $\odot$ symbolises the Hadamard product, and $mask_x$ is a binary matrix at the coordinate (i,j), defined by

$$mask_x(i,j) = \begin{cases} 1, & \text{if } (i,j) \in P_x, \\ 0, & \text{otherwise}, \end{cases} \quad (17)$$

where P_x represents the subset of x-channel.

The correction of each channel estimate is performed individually. Considering the 0° channel as an example, we initially computed the sparse differential estimation plane relative to the 0° channel for the other three channels at the positions P_0 as follows:

$$\widetilde{\Delta}_{c,0} = \widetilde{\mathbf{M}}_0 - \widehat{I}_c \odot mask_0, \quad c \in \{45, 90, 135\}. \quad (18)$$

Under the assumption of neighbour channel difference consistency [22], bilinear interpolation is used to obtain three complete difference planes:

$$\widehat{\Delta}_{c,0} = \widetilde{\Delta}_{c,0} * F, \quad c \in \{45, 90, 135\}. \quad (19)$$

Next, the correction of each channel to the 0° channel is obtained by summing the estimation planes with the difference planes of the corresponding channels:

$$\widehat{I}_{c,0} = \widehat{I}_c + \widehat{\Delta}_{c,0}, \quad c \in \{45, 90, 135\}. \quad (20)$$

The final refinement for the 0° channel is achieved through the weighted mean of the three individual channel corrections mentioned above:

$$I_0 = \sum_c \omega_c \widehat{I}_{c,0}, \quad (21)$$

where c denotes the other three channels, i.e., $c \neq 0$. ω_c denotes the weight of the c -channel, with $\sum_c \omega_c = 1$. As horizontal and vertical channels have an equal and more substantial influence than orthogonal channels, (21) can be simplified as follows:

$$I_0 = \omega_{hv}(\widehat{I}_{45,0} + \widehat{I}_{135,0}) + \omega_{orth}\widehat{I}_{90,0}, \quad (22)$$

TABLE I
TECHNICAL DESCRIPTIONS OF 11 POLARIZATION DEMOSAICKING METHODS

Method	Interpolation Decision	Initial Estimation	Calibration
NN	No	Nearest-Neighbor Interpolation	No
BI	No	Bilinear Interpolation	No
BCB	No	Bicubic Interpolation	No
ICPC	Edge Binary Decision	Bicubic Spline Interpolation	No
EARI	Directional-Conv Edge-aware	Residual Interpolation	No
PCDP	No	Bilinear Interpolation	Inter-Channel Correlation
PDEC	No	Bilinear & Edge Compensation	Inter-Channel Correlation
Huber2d	No	ADMM Stokes Optimization	No
NP	Weighted Edge Classifier	Newton's Polynomial Interpolation	No
LEPD	Logistic DLE	Hamilton–Adam Interpolation	No
LEIC	Logistic DLE	Hamilton–Adam Interpolation	Inter-Channel Correlation

TABLE II
AVERAGE PSNR ON SIMULATED IMAGES

PSNR	NN	BI	BCB	ICPC	EARI	PCDP	PDEC	Huber2d	NP	LEPD	LEIC
I_0	36.502	41.049	42.022	41.768	41.604	43.128	43.245	43.021	**43.664**	**43.575**	**44.314**
I_{45}	38.149	43.031	43.823	43.784	43.397	44.970	45.107	44.569	**45.323**	**45.345**	**46.079**
I_{90}	38.197	43.243	43.875	43.988	43.384	**45.171**	45.121	44.982	44.907	**45.259**	**45.870**
I_{135}	37.543	42.270	43.021	42.968	42.589	44.395	44.610	44.014	**45.206**	**44.958**	**45.705**
S_0	40.332	44.727	45.711	45.673	45.130	46.911	47.033	46.732	**48.254**	**47.900**	**48.406**
DoLP	32.748	38.113	38.849	39.009	38.748	39.743	**39.880**	39.211	38.806	**39.822**	**40.033**
AoLP	23.207	26.144	25.990	26.319	26.198	26.750	27.035	27.133	**27.159**	**27.232**	**27.410**

where ω_{hv} denotes the horizontal and vertical channel weights, and ω_{orth} denotes the orthogonal channel weights with $2\omega_{hv} + \omega_{orth} = 1$. The values of these weights correlate with their contribution to the final image, with a theoretical bias, such that, $\omega_{hv} > \omega_{orth}$. The global weights are deduced from the polarization distance [22] as follows:

$$\begin{cases} \omega_{hv} = \frac{\sqrt{2}}{1+2\sqrt{2}}, \\ \omega_{orth} = \frac{1}{1+2\sqrt{2}}. \end{cases} \tag{23}$$

The outlined ICCC method can be easily extended to the other three channels to obtain all four calibrated images. Therefore, a detailed exposition of this procedure is omitted here.

The introduction of ICCC significantly improves interpolation accuracy and effectively eliminates redundant textures, as discussed in Section III.

F. Polarization Demosaicking Using LEIC and LEPD

Finally, we integrate the computational steps described above to introduce a novel polarization demosaicking algorithm, LEIC. The algorithm flow and a visual representation of LEIC, along with its lightweight version, LEPD, are depicted in Algorithm 1 and Fig. 3, respectively.

IV. EXPERIMENTS

In this section, we design two experiments to assess the performance of our LEPD and LEIC algorithms. In the first experiment, we compare the quantitative metrics, visual effects, and running speeds of different demosaicking methods using simulated DoFP images. Subsequently, the methods are tested on a self-built real DoFP images dataset, the OLVD [35]. Traditional methods, such as NN, BI, and BCB [18], and advanced methods such as ICPC [19], EARI [21], PCDP [22], PDEC [23], Huber2d [31], NP [20], have been used for comparison against our LEPD and LEIC. It is important to emphasize that this paper primarily focuses on real-time demosaicking algorithms for monochrome polarization filter arrays (MPFA). Therefore, experiments involving color polarization filter arrays (CPFA) and data-driven demosaicking algorithms [36], [37], [38] are not considered.

The technical descriptions of these methods are presented in Table I. The complete code for PCDP, PDEC, ICPC, EARI, Huber2d and NP is publicly available from the authors, and NN, BI, and BCB are written in MATLAB software. All experiments run on computer systems with an AMD Ryzen 5600x CPU and NVIDIA RTX 2070 graphics processing unit.

A. Performance Assessment on Simulated Images

Using the time-shifted polarization image dataset provided by Qiu et al. [31], we synthesised simulated DoFP images with a resolution of 1024 × 1024, as shown in Fig. 5. Images from the four polarization channels at full resolution are downsampled following the MPFA pattern and subsequently fused to create a simulated DoFP image (Fig. 6).

Algorithm 1: Proposed LEIC Method.

Input: DoFP raw image; Version (LEPD or LEIC)
Output: Demosaicked images I_0, I_{45}, I_{90}, and I_{135}

// Step 1. Estimate Orthogonal Channel Plane by DLE
Compute the diagonal and anti-diagonal weights, ω_d and ω_a, by Eq. (4a) to (4d), (5a), (5b), (9a), and (9b).
Estimate the value of the orthogonal channel plane $\widehat{I}_{orth}$ using Eq. (4b), (4d), (6a), (6b), (7), ω_d, and ω_a.
// Step 2. Estimate Non-orthogonal Channel Plane by DLE
Calculate the orthogonal channel difference map $\widehat{\Delta}_{orth}$ by Eq. (10).
Calculate the horizontal and vertical weights, ω_h and ω_v, by Eq. (11a)∼(11d), (12a), (12b), (15c), and (15d).
Estimate the value of horizontal and vertical channel plane, $\widehat{I}_h$ and $\widehat{I}_v$, using Eq. (13a) to (13d), (14a), (14b), (15a), (15b), ω_h, and ω_v.
Generate four demosaicked images (I_0, I_{45}, I_{90}, and I_{135}) by extracting corresponding values from $\mathbf{M}$, $\widehat{I}_{orth}$, $\widehat{I}_h$, and $\widehat{I}_v$.
if version is LEPD **then**
  return I_0, I_{45}, I_{90}, and I_{135}. **(The lightweight version: LEPD)**
end
// Step 3. Update with Observed Data by ICCC
foreach channel x **do**
  Compute the difference plane of the other 3 channels $\widehat{\Delta}_{c,x}$ using Eq. (16) to (19);
  Compute the corrections for the other 3 channels $\widehat{I}_{c,x}$ using Eq. (20);
  Refine the demosaicked images for channel x, I_x, using Eq. (22) with global channel weights ω_{hv} and ω_{orth} as defined in Eq. (23).
end
return I_0, I_{45}, I_{90}, and I_{135}. **(The full version: LEIC)**

The simulated DoFP images from 40 scenes in the dataset were demosaicked using the aforementioned 11 methods. The average PSNR, RMSE, and SSIM results are presented in Tables II, III, and IV, respectively. These metrics assess convey signal fidelity (PSNR), accuracy of value estimation (RMSE), and similarity between two images (SSIM). In each table, the top three results are highlighted in red, green, and blue to indicate the best, second-best, and third-best outcomes, respectively.

In these quantitative tests, our LEIC method consistently produces superior results across most metrics. Compared with LEIC, the PDEC method exhibits improved RMSE and SSIM scores on $DoLP$ but underperforms in other metrics. Overall, NP is ranked as the second-best method following LEIC; however, it demonstrates particularly inferior performance in reconstructed $DoLP$ images across all metrics. LEIC significantly outperforms NP, which also employs edge-aware techniques.

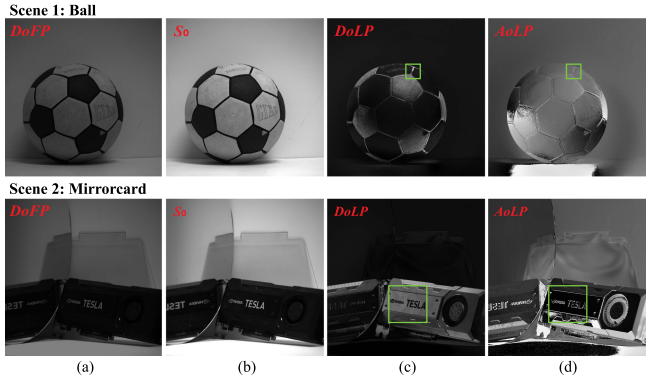

Fig. 5. Selected scenes (Ball and Mirrorcard) from Qiu's dataset [31] applied in the test experiments. (a) Simulated DoFP images; (b) S_0 images; (c) $DoLP$ images; (d) $AoLP$ images.

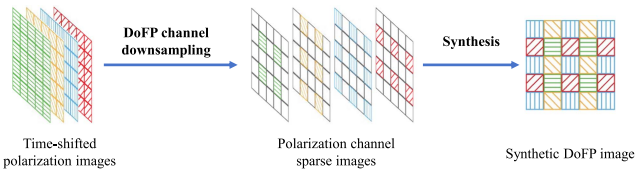

Fig. 6. Simulation process of DoFP images using time-shifted polarization images.

Additionally, the LEPD also performs well in most metrics, affirming the high efficacy of our reconstruction strategy, even without the calibration process.

Next, we evaluated demosaicking performance by comparing interpolated images with actual images, as shown in Fig. 7. These images are acquired from the green boxed sections of Fig. 5. For enhanced visual comparisons, DoLP and AoLP images were pseudo-coloured using parula and HSV colour maps, respectively. Compared with other methods, our methods and NP effectively suppress zipper artefacts around high-frequencies highlighting the importance of directionality in interpolation decisions. However, NP significantly relies on orthogonal interpolation, which tends to exaggerate textures, introduce artifactual x-like patterns, and reduce detail sharpness, as shown in Fig. 7(h). By contrast, our LEPD and LEIC methods exhibit significant refinements on these issues. Moreover, compared with LEPD, LEIC employs ICCC to enhance fidelity by filtering out certain redundant interpolated textures, further improving the quality and clarity of the images.

Finally, the running times of the various demosaicking methods are evaluated, as presented in Table V. Notably, traditional methods such as NN, BI, and BCB are excluded from the speed comparisons because of their unsatisfactory performance quality. NP demonstrates robust performance in previous tests but incurs significant computational costs because of its complex interpolation decision-making process and the large computation window required. The optimization-based Huber2d method has the longest runtime, with the duration of a single iteration already surpassing that of all other interpolation methods. By contrast,

TABLE III
AVERAGE RMSE ON SIMULATED IMAGES

RMSE	NN	BI	BCB	ICPC	EARI	PCDP	PDEC	Huber2d	NP	LEPD	LEIC
I_0	3.2020	1.8842	1.7533	1.7498	1.8218	1.4969	1.4827	1.5540	**1.4340**	**1.4243**	**1.3281**
I_{45}	2.8468	1.6157	1.4871	1.4722	1.5593	1.2400	1.2173	1.2653	**1.1957**	**1.1827**	**1.0878**
I_{90}	2.8597	1.5664	1.4802	1.4270	1.5672	**1.1988**	1.2021	1.2432	1.2569	**1.1869**	**1.1102**
I_{135}	3.0967	1.8040	1.7024	1.6782	1.7767	1.4198	1.3886	1.4768	**1.3145**	**1.3321**	**1.2406**
S_0	2.0540	1.2287	1.1338	1.1053	1.2057	0.9386	0.9267	0.9862	**0.8043**	**0.8325**	**0.7945**
DoLP	0.0266	0.0146	0.0135	0.0132	0.0134	0.0122	**0.0120**	0.0125	0.0145	**0.0121**	**0.0121**
AoLP	0.0798	0.0621	0.0608	0.0619	0.0591	0.0582	0.0565	0.0560	**0.0545**	**0.0550**	**0.0538**

TABLE IV
AVERAGE SSIM ON SIMULATED IMAGES

SSIM	NN	BI	BCB	ICPC	EARI	PCDP	PDEC	Huber2d	NP	LEPD	LEIC
I_0	0.5921	0.5921	0.5933	0.5724	0.6130	0.6598	0.6606	0.6478	**0.7158**	**0.7120**	**0.7303**
I_{45}	0.5842	0.5842	0.5858	0.5650	0.6118	0.6509	0.6569	0.6542	**0.7116**	**0.7089**	**0.7256**
I_{90}	0.5819	0.5819	0.5828	0.5630	0.6123	0.6465	0.6470	0.6367	**0.6936**	**0.6970**	**0.7087**
I_{135}	0.5874	0.5874	0.5917	0.5676	0.6125	0.6566	0.6590	0.6469	**0.7174**	**0.7113**	**0.7310**
S_0	0.6657	0.6657	0.6768	0.6515	0.6983	0.7415	0.7386	0.7447	**0.8115**	**0.8066**	**0.8148**
DoLP	0.9294	0.9294	0.9309	0.9322	0.9342	0.9391	**0.9413**	0.9303	0.9298	**0.9400**	**0.9392**
AoLP	0.6861	0.6861	0.6786	0.6778	0.6918	0.7039	0.7193	0.7306	**0.7378**	**0.7318**	**0.7382**

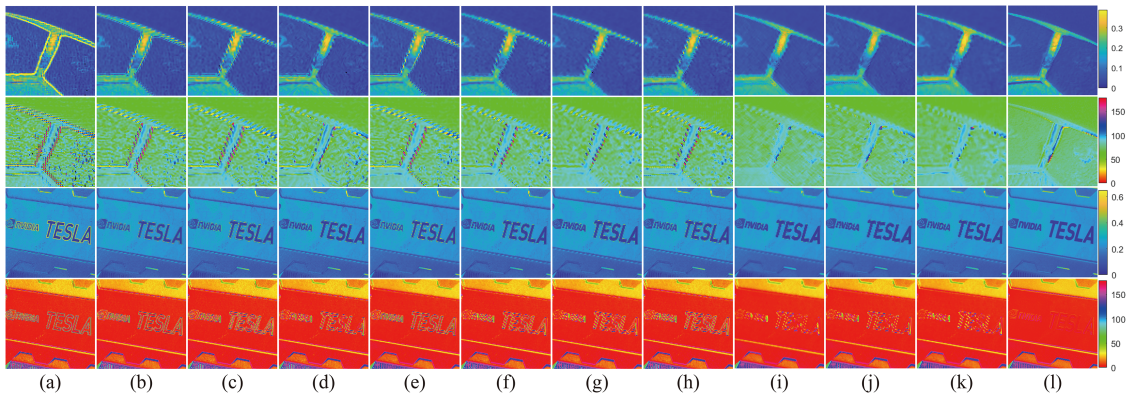

Fig. 7. Visual comparison of polarization image reconstruction using different demosaicking techniques. From left to right, the reconstruction results are from methods (a) NN, (b) BI, (c) BCB, (d) ICPC, (e) EARI, (f) PCDP, (g) PDEC, (h) Huber2d, (i) NP, (j) LEPD, (k) LEIC, and (l) ground-truth, respectively.

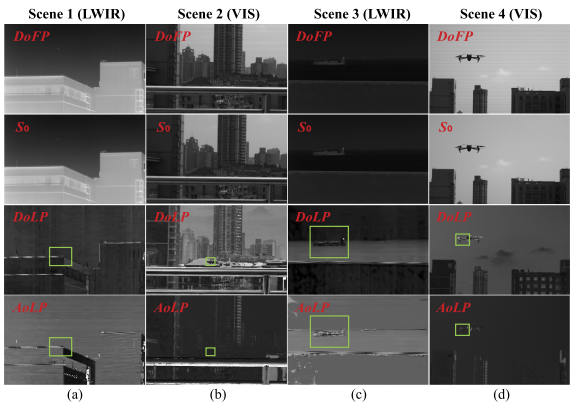

Fig. 8. Four real DoFP scenes of OLVD; certain scenes include distant targets such as ships or UAVs. Rows 1 to 4 display DoFP, S_0, $DoLP$, and $AoLP$ images, respectively.

TABLE V
RUNNING TIME ON SIMULATED DOFP IMAGES

Method	ICPC	EARI	PCDP	PDEC	Huber2d	NP	LEPD	LEIC
Time (*s*)	0.4648	1.3166	**0.1895**	**0.2610**	2.8350	0.5186	**0.1402**	0.2693

our LEPD method exhibits the fastest speed, being 26% faster than the second-fastest method, PCDP. Our LEIC method builds upon LEPD and incorporates ICCC, which includes certain additional time costs but achieves the best overall interpolation performance. The running time of LEIC is comparable to that of PDEC and is significantly lower than those of NP and EARI by 92.46% and 388.90%, respectively. This efficiency in processing time, coupled with superior image quality, highlights the effectiveness of our LEIC method in balancing performance with computational efficiency.

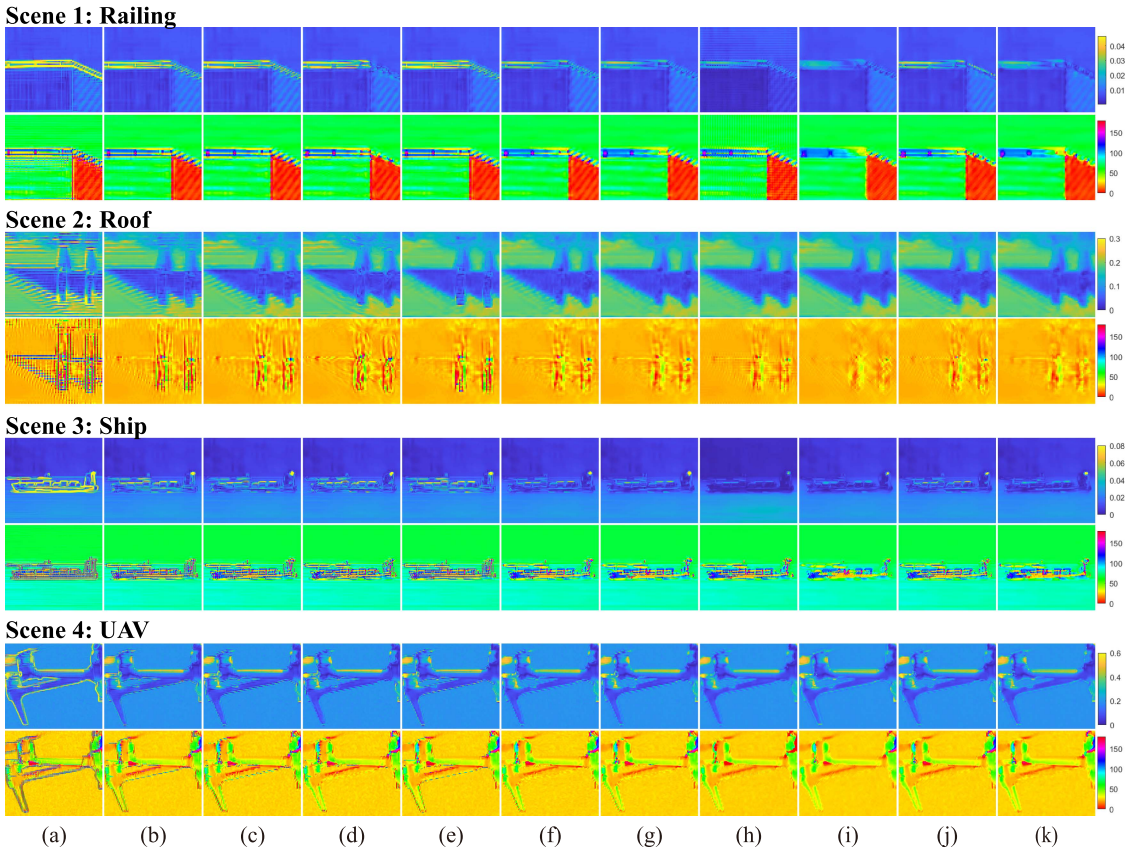

Fig. 9. Visual comparison of demosaicking methods on real DoFP images. The first and second rows in each scene correspond to $DoLP$ and $AoLP$, respectively. From left to right, the reconstruction results are presented by methods (a) NN, (b) BI, (c) BCB, (d) ICPC, (e) EARI, (f) PCDP, (g) PDEC, (h) Huber2d, (i) NP, (j) our LEPD and (k) LEIC.

B. Test on Real DoFP Images

In this experiment, we selected four real DoFP images from our OLVD [35] for testing, as displayed in Fig. 8. Scenes 1 and 3 were captured using the North Guangwei UMC4A-PU0A Micro DoFP LWIR polarization imager. This device incorporates an array of wire-grid micro-polarizers [39], features a resolution of 640 $\times$ 512, and records images with a depth of 14 bits. Scenes 2 and 4 were captured using the Daheng Imaging MER2-503-36U3M POL DoFP visible polarization imager, which utilizes a monochromatic quad-polarizer array [40]. This imager operates at a resolution of 2448 $\times$ 2048, an 8-bit depth, and a frame rate of 36 fps. Additionally, the pBM3D method [41] was employed to denoise the DoFP images, ensuring the enhancement of image quality by reducing noise while preserving important polarization information.

Fig. 9 illustrates the $DoLP$ and $AoLP$ results using various MPFA demosaicking methods for the green boxed areas of Fig. 8. For enhanced visual comparison, similar to Fig. 6, the $DoLP$ and $AoLP$ images are processed in parula and HSV pseudo-colors, respectively.

Traditional demosaicking methods, as shown in Fig. 9(a), (b), and (c), produce significant artifacts in both LWIR and VIS DoFP images. Advanced methods achieve varying degrees of artifact mitigation. Edge-aware-based methods such as ICPC, EARI, and NP reduce false edges to some extent. However, they share a common issue of injecting redundant false textures due to the instability of the interpolation decision maker, as demonstrated in Fig. 9(d), (e), and (i). A typical example includes the x-like textures produced by NP, notably visible in scenes 1 and 2 of Fig. 9(i). PCDP and PDEC reduce incorrect high-frequency information through multi-channel difference domain interpolation; however, the absence of directional interpolation decisions often leads to significant artifacts, as evident in Fig. 9(f) and (g). Huber2d effectively recovers $DoLP$ and $AoLP$ using an optimization-based strategy, resulting in quantized values that closely resemble the ground truth, as shown in Fig. 9(h). However, a significant "zip" effect remains in high-frequency regions, and parameters, such as the optimal number of iterations, still need to be manually configured.

In contrast, LEPD matches or even surpasses the performance of PCDP and PDEC in artifact treatment, such as those observed around the UAV in scene 4 of Fig. 9(j). By employing ICCC, LEIC further diminishes artifacts and false textures. LEIC's performance is comparable to that of NP but with minimal additional textural errors. In summary, LEIC significantly enhances the fidelity and visualization of reconstructed polarization images.

Finally, Table VI lists the runtimes of various high-precision demosaicking methods on the DoFP images of LWIR and VIS.

TABLE VI
RUNNING TIME ON REAL DOFP IMAGES

Time (*s*)	ICPC	EARI	PCDP	PDEC	Huber2d	NP	LEPD	LEIC
LWIR	0.1393	0.3229	0.0629	0.0807	0.7760	0.1512	0.0405	0.0935
VIS	3.1531	9.0719	1.1519	1.5329	14.267	2.7124	0.8014	1.7440

Note that the time indicated for Huber2d in the table represents the duration of a single iteration. Among them, LEPD is the fastest, while LEIC offers the best reconstruction performance with satisfactory computational costs, balancing efficiency with effectiveness in processing DoFP images.

V. CONCLUSION

We introduce an efficient LEIC method for demosaicking images captured by DoFP sensors, known as LEIC. This method is based on a standardized framework called the TIPDF. LEIC incorporates a low-cost edge-aware strategy, termed DLE, that guides the interpolation process using a Logistic function to account for differences in directional variations. Additionally, LEIC utilizes an ICCC technique to refine the demosaicked results. For applications requiring a less resource-intensive solution, we propose LEPD as a lightweight version of LEIC, which omits the ICCC component. Among 10 tested interpolation-based demosaicking methods, LEIC emerged as superior in quantitative metrics and visual effects while maintaining low computational costs. Meanwhile, LEPD ranks as the swiftest among the non-traditional methods. In scenarios where accuracy is prioritized over speed, LEPD can serve as a rapid, high-quality initializer for more complex DoFP demosaicking programs. Owing to their high parallelizability, our methods can recover high-resolution images in real-time on GPUs or FPGAs, rendering them highly suitable for industrial applications.

Moreover, there remains room for further enhancement of our methods. Specifically, within certain high-frequency edge zones of images, "zip" effects are not entirely abolished, even though the pseudo-edge is suppressed. Such limitations could arguably be attributed to the simplicity of the decision-making mechanism for interpolated direction and the global characteristic of the ICCC. Future optimizations to improve image quality and decrease performance overhead could conceivably entail the creation of more sophisticated weight calculation functions and the application of selective calibrations. Besides, with further improvements, our algorithm is expected to efficiently perform demosaicking of color polarization filter arrays (CPFA).

REFERENCES

[1] A. Z. Kechiche, O. Aubreton, A. Mathieu, A. Mannucci, and C. Stolz, "Polarimetric imaging method for surface quality evaluation of a liquid metal pool obtained during welding," *Opt. Eng.*, vol. 59, no. 10, pp. 100501–100501, 2020.

[2] X. Li, F. Liu, P. Han, S. Zhang, and X. Shao, "Near-infrared monocular 3D computational polarization imaging of surfaces exhibiting nonuniform reflectance," *Opt. Exp.*, vol. 29, no. 10, pp. 15616–15630, 2021.

[3] K. Usmani, G. Krishnan, T. O'Connor, and B. Javidi, "Deep learning polarimetric three-dimensional integral imaging object recognition in adverse environmental conditions," *Opt. Exp.*, vol. 29, no. 8, pp. 12215–12228, 2021.

[4] N. Li, Y. Zhao, Q. Pan, S. G. Kong, and J. C.-W. Chan, "Illumination-invariant road detection and tracking using LWIR polarization characteristics," *ISPRS J. Photogrammetry Remote Sens.*, vol. 180, pp. 357–369, 2021.

[5] J. M. Romano, D. Rosario, and J. McCarthy, "Day/night polarimetric anomaly detection using SPICE imagery," *IEEE Trans. Geosci. Remote Sens.*, vol. 50, no. 12, pp. 5014–5023, Dec. 2012.

[6] D. Zhu and W. A. Smith, "Depth from a polarisation RGB stereo pair," in *Proc. IEEE/CVF Conf. Comput. Vis. Pattern Recognit.*, 2019, pp. 7586–7595.

[7] F. Hu et al., "Polarization-based material classification technique using passive millimeter-wave polarimetric imagery," *Appl. Opt.*, vol. 55, no. 31, pp. 8690–8697, 2016.

[8] Z. Liang, X. Ding, Z. Mi, Y. Wang, and X. Fu, "Effective polarization-based image dehazing with regularization constraint," *IEEE Geosci. Remote Sens. Lett.*, vol. 19, 2020, Art. no. 8001405.

[9] M. Garcia et al., "Bio-inspired imager improves sensitivity in near-infrared fluorescence image-guided surgery," *Optica*, vol. 5, no. 4, pp. 413–422, 2018.

[10] Y. Niu, J. Ouyang, W. Zuo, and F. Wang, "Low cost edge sensing for high quality demosaicking," *IEEE Trans. Image Process.*, vol. 28, no. 5, pp. 2415–2427, May 2018.

[11] J. Wu, M. Anisetti, W. Wu, E. Damiani, and G. Jeon, "Bayer demosaicking with polynomial interpolation," *IEEE Trans. Image Process.*, vol. 25, no. 11, pp. 5369–5382, Nov. 2016.

[12] X. Yang, W. Zhou, and H. Li, "MCFD: A hardware-efficient noniterative multicue fusion demosaicing algorithm," *IEEE Trans. Circuits Syst. Video Technol.*, vol. 31, no. 9, pp. 3575–3589, Sep. 2021.

[13] C.-Y. Lien, F.-J. Yang, and P.-Y. Chen, "An efficient edge-based technique for color filter array demosaicking," *IEEE Sensors J.*, vol. 17, no. 13, pp. 4067–4074, Jul. 2017.

[14] D. Menon, S. Andriani, and G. Calvagno, "Demosaicing with directional filtering and a posteriori decision," *IEEE Trans. Image Process.*, vol. 16, no. 1, pp. 132–141, Jan. 2007.

[15] D. Kiku, Y. Monno, M. Tanaka, and M. Okutomi, "Beyond color difference: Residual interpolation for color image demosaicking," *IEEE Trans. Image Process.*, vol. 25, no. 3, pp. 1288–1300, Mar. 2016.

[16] S. Mihoubi, P.-J. Lapray, and L. Bigué, "Survey of demosaicking methods for polarization filter array images," *Sensors*, vol. 18, no. 11, 2018, Art. no. 3688.

[17] B. M. Ratliff, C. F. LaCasse, and J. S. Tyo, "Interpolation strategies for reducing IFOV artifacts in microgrid polarimeter imagery," *Opt. Exp.*, vol. 17, no. 11, pp. 9112–9125, 2009.

[18] S. Gao and V. Gruev, "Bilinear and bicubic interpolation methods for division of focal plane polarimeters," *Opt. Exp.*, vol. 19, no. 27, pp. 26161–26173, 2011.

[19] J. Zhang, H. Luo, B. Hui, and Z. Chang, "Image interpolation for division of focal plane polarimeters with intensity correlation," *Opt. Exp.*, vol. 24, no. 18, pp. 20799–20807, 2016.

[20] N. Li, Y. Zhao, Q. Pan, and S. G. Kong, "Demosaicking DoFP images using Newton's polynomial interpolation and polarization difference model," *Opt. Exp.*, vol. 27, no. 2, pp. 1376–1391, 2019.

[21] M. Morimatsu, Y. Monno, M. Tanaka, and M. Okutomi, "Monochrome and color polarization demosaicking using edge-aware residual interpolation," in *Proc. 2020 IEEE Int. Conf. Image Process.*, 2020, pp. 2571–2575.

[22] R. Wu, Y. Zhao, N. Li, and S. G. Kong, "Polarization image demosaicking using polarization channel difference prior," *Opt. Exp.*, vol. 29, no. 14, pp. 22066–22079, 2021.

[23] J. Xin, Z. Li, S. Wu, and S. Wang, "Demosaicking DoFP images using edge compensation method based on correlation," *Opt. Exp.*, vol. 31, no. 9, pp. 13536–13551, 2023.

[24] J. Zhang et al., "Sparse representation-based demosaicing method for microgrid polarimeter imagery," *Opt. Lett.*, vol. 43, no. 14, pp. 3265–3268, 2018.

[25] N. Li, B. Wang, F. Goudail, Y. Zhao, and Q. Pan, "Joint denoising-demosaicking network for long-wave infrared division-of-focal-plane polarization images with mixed noise level estimation," *IEEE Trans. Image Process.*, vol. 32, pp. 5961–5976, 2023.

[26] X. Zeng, Y. Luo, X. Zhao, and W. Ye, "An end-to-end fully-convolutional neural network for division of focal plane sensors to reconstruct S_0, DoLP, and AoP," *Opt. Exp.*, vol. 27, no. 6, pp. 8566–8577, 2019.

[27] M. Pistellato, F. Bergamasco, T. Fatima, and A. Torsello, "Deep demosaicing for polarimetric filter array cameras," *IEEE Trans. Image Process.*, vol. 31, pp. 2017–2026, 2022.
[28] J. F. Hamilton Jr, "Adaptive color plan interpolation in signal sensor color electronic camera," United State Patent, 5,629,734, 1997.
[29] A. Buades, B. Coll, J.-M. Morel, and C. Sbert, "Self-similarity driven color demosaicking," *IEEE Trans. Image Process.*, vol. 18, no. 6, pp. 1192–1202, Jun. 2009.
[30] M. Gharbi, G. Chaurasia, S. Paris, and F. Durand, "Deep joint demosaicking and denoising," *ACM Trans. Graph.*, vol. 35, no. 6, pp. 1–12, 2016.
[31] S. Qiu, Q. Fu, C. Wang, and W. Heidrich, "Polarization demosaicking for monochrome and color polarization focal plane arrays," in *Proc. Int. Symp. Vis., Model. Vis., Eurographics Assoc.*, 2019.
[32] B. Sun, N. Yuan, and Z. Zhao, "A hybrid demosaicking algorithm for area scan industrial camera based on fuzzy edge strength and residual interpolation," *IEEE Trans. Ind. Informat.*, vol. 16, no. 6, pp. 4038–4048, Jun. 2020.
[33] X. Li, B. Gunturk, and L. Zhang, "Image demosaicing: A systematic survey," in *Visual Communications and Image Processing*, vol. 6822. Bellingham, WA, USA: SPIE, 2008, pp. 489–503.
[34] K.-H. Chung and Y.-H. Chan, "Color demosaicing using variance of color differences," *IEEE Trans. Image Process.*, vol. 15, no. 10, pp. 2944–2955, Oct. 2006.
[35] L. Guangsen, "OLVD dataset," (n.d). [Online]. Available: https://github.com/lgs195/OLVD
[36] V. Nguyen, M. Tanaka, Y. Monno, and M. Okutomi, "Two-step color-polarization demosaicking network," in *Proc. 2022 IEEE Int. Conf. Image Process.*, 2022, pp. 1011–1015.
[37] A. Spote, P.-J. Lapray, J.-B. Thomas, and I. Farup, "Joint demosaicing of colour and polarisation from filter arrays," in *Proc. Color Imag. Conf.*, 2021, pp. 288–293.
[38] R. Dumoulin, P.-J. Lapray, J.-B. Thomas, and I. Farup, "Impact of training data on LMMSE demosaicing for colour-polarization filter array," in *Proc. 2022 16th Int. Conf. Signal-Image Technol. Internet-Based Syst.*, IEEE, 2022, pp. 275–280.
[39] Z. Yongqiang, L. Ning, Z. Peng, Y. Jiaxin, and P. Quan, "Infrared polarization perception and intelligent processing," *Infrared Laser Eng.*, vol. 47, no. 11, 2018, Art. no. 1102001.
[40] S. Group et al., "Polarization image sensor with four-directional on-chip polarizer and global shutter function,".
[41] A. Abubakar, X. Zhao, S. Li, M. Takruri, E. Bastaki, and A. Bermak, "A block-matching and 3-D filtering algorithm for Gaussian noise in DoFP polarization images," *IEEE Sensors J.*, vol. 18, no. 18, pp. 7429–7435, Sep. 2018.